

Accurate and Efficient Evaluation of Characteristic Modes

Doruk Tayli, *Student Member, IEEE*, Miloslav Capek, *Member, IEEE*, Lamyae Akrou, Vit Losenicky, Lukas Jelinek, and Mats Gustafsson, *Senior Member, IEEE*

Abstract—A new method to improve the accuracy of characteristic modes decomposition for perfectly conducting bodies is presented. The method uses the expansion of the Green dyadic in spherical vector waves. This expansion is utilized in the method of moments solution of the electric field integral equation to improve the numerical range of the real part of the impedance matrix, \mathbf{R} , that determines the number of obtainable modes from characteristic modes decomposition. Computation speed of the \mathbf{R} matrix and characteristic modes are improved. The method can easily be integrated in existing method of moments solvers. Several structures are investigated illustrating the improved accuracy and performance of the new method.

Index Terms—Antenna theory, numerical analysis, eigenvalues and eigenfunctions, electromagnetic theory, convergence of numerical methods.

I. INTRODUCTION

THE method of moments (MoM) solution to electromagnetic field integral equations was introduced by Harrington [1] and has prevailed as a standard in solving open (radiating) electromagnetic problems [2]. While memory-demanding, MoM represents operators as matrices (notably the impedance matrix [1]) allowing for direct inversion and modal decompositions [3]. The latter option is becoming increasingly popular, mainly due to characteristic mode (CM) decomposition [4], a leading formalism in antenna shape and feeding synthesis [5], [6], determination of optimal currents [7], [8], and performance evaluation [9].

Utilization of CMs decomposition is especially efficient when dealing with electrically small antennas [10], particularly if they are made solely of perfect electric conductor (PEC), for which only a small number of modes are needed to describe their radiation behavior. Yet, decompositions involving the real part of impedance matrix are known [4], [11] to be ill conditioned for electrically small structures, since only a few modes radiate well, while the rest is numerical noise [11]. This

drawback affects the performance of CMs decomposition and prohibits the superposition of modes [6].

The aforementioned deficiency is resolved in this paper by a two-step procedure. First, the real part of the impedance matrix is constructed using spherical wave expansion of the dyadic Green function [12]. This makes it possible to decompose the real part of the impedance matrix as a product of a spherical modes projection matrix with its hermitian conjugate. The second step consists of reformulating the modal decomposition so that only the stand alone spherical modes projection matrix is involved. This avoids the loss of attainable numerical dynamics during the matrix multiplication process.

The proposed implementation doubles the numerical accuracy with respect to the used arithmetic precision in computing, significantly increasing the number of correctly found modes. For example, the proposed procedure yields more than 280 modes versus 70 modes reported in [11] on a spherical shell (at given electrical size). The improvement in correctly found modes is also accompanied by an additional computation speed. Moreover, the projection on spherical waves in the proposed method introduces several appealing properties. First is an easy monitoring of the numerical dynamics, since the different spherical waves (of different numerical dynamics) occupy separate rows in the projection matrix. Second is the ability to control the spectrum of impedance matrix which plays important role in an optimal design [8].

The paper is organized as follows. The construction of the impedance matrix using classical procedure is briefly reviewed in Section II-A and the proposed procedure is presented in Section II-B. Numerical aspects of evaluating the impedance matrix are discussed in Section II-C. In Section III, the spherical modes projection matrix is utilized to reformulate modal decomposition techniques, namely the evaluation of radiation modes in Section III-A and CMs in Section III-B. These two applications cover both the standard and generalized eigenvalue problems. The advantages of the proposed procedure are demonstrated on a series of practical examples in this section. Various aspects of the proposed method are discussed in Section IV and the paper is concluded in Section V.

II. EVALUATION OF IMPEDANCE MATRIX

This paper investigates mode decompositions for PEC structures in free space. The time-harmonic quantities under the convention $\mathcal{J}(\mathbf{r}, t) = \text{Re}\{\mathbf{J}(\mathbf{r}, \omega) \exp(j\omega t)\}$, with ω being the angular frequency, are used throughout the paper.

Manuscript received December 14, 2024; revised December 14, 2024. This work was supported by the Swedish Foundation for Strategic Research (SSF) under the program Applied Mathematics and the project Complex analysis and convex optimization for EM design, and by the Czech Science Foundation under project No. 15-10280Y.

D. Tayli and M. Gustafsson are with the Department of Electrical and Information Technology, Lund University, 221 00 Lund, Sweden (e-mail: {doruk.tayli,mats.gustafsson}@eit.lth.se).

M. Capek, V. Losenicky and L. Jelinek are with the Department of Electromagnetic Field, Faculty of Electrical Engineering, Czech Technical University in Prague, Technicka 2, 166 27 Prague, Czech Republic (e-mail: {miloslav.capek,losevenvit,lukas.jelinek}@fel.cvut.cz).

L. Akrou is with the Department of Electrical and Computer Engineering, Faculty of Sciences and Technology, University of Coimbra, Polo II, Pinhal de Marrocos, 3030-290 Coimbra, Portugal (e-mail: lakrou@co.it.pt).

A. Method of Moments Implementation of the EFIE

Let us consider the electric field integral equation (EFIE) [1] for PEC bodies, defined as

$$\mathcal{Z}(\mathbf{J}) = \mathcal{R}(\mathbf{J}) + j\mathcal{X}(\mathbf{J}) = \hat{\mathbf{n}} \times (\hat{\mathbf{n}} \times \mathbf{E}), \quad (1)$$

with $\mathcal{Z}(\mathbf{J})$ being the impedance operator, \mathbf{E} the incident electric field [13], \mathbf{J} the current density, j the imaginary unit, and $\hat{\mathbf{n}}$ the unit normal vector to the PEC surface. The EFIE (1) is explicitly written as

$$\hat{\mathbf{n}} \times \mathbf{E}(\mathbf{r}_2) = jkZ_0 \hat{\mathbf{n}} \times \int_{\Omega} \mathbf{G}(\mathbf{r}_1, \mathbf{r}_2) \cdot \mathbf{J}(\mathbf{r}_1) dS_1, \quad (2)$$

where $\mathbf{r}_2 \in \Omega$, k is the wave number, Z_0 the free space impedance, and \mathbf{G} the dyadic Green function for the electric field in free-space defined as [12], [14]

$$\mathbf{G}(\mathbf{r}_1, \mathbf{r}_2) = \left(\mathbf{1} + \frac{1}{k^2} \nabla \nabla \right) \frac{e^{-jk|\mathbf{r}_1 - \mathbf{r}_2|}}{4\pi |\mathbf{r}_1 - \mathbf{r}_2|}. \quad (3)$$

Here, $\mathbf{1}$ is the identity dyadic, and $\mathbf{r}_1, \mathbf{r}_2$ are the source and observation points. The EFIE (2) is solved with the MoM by expanding the current density $\mathbf{J}(\mathbf{r})$ into real-valued basis functions $\{\psi_p(\mathbf{r})\}$ as

$$\mathbf{J}(\mathbf{r}) \approx \sum_{p=1}^{N_\psi} I_p \psi_p(\mathbf{r}) \quad (4)$$

and applying Galerkin testing procedure [14], [15]. The impedance operator $\mathcal{Z}(\mathbf{J})$ is expressed as the impedance matrix $\mathbf{Z} = \mathbf{R} + j\mathbf{X} = [Z_{pq}] \in \mathbb{C}^{N_\psi \times N_\psi}$, where \mathbf{R} is the resistance matrix, and \mathbf{X} the reactance matrix. The elements of the impedance matrix are

$$Z_{pq} = jkZ_0 \int_{\Omega} \int_{\Omega} \psi_p(\mathbf{r}_1) \cdot \mathbf{G}(\mathbf{r}_1, \mathbf{r}_2) \cdot \psi_q(\mathbf{r}_2) dS_1 dS_2. \quad (5)$$

B. Spherical Wave Expansion of the Green Dyadic

The impedance matrix \mathbf{Z} can alternatively be computed by expanding the Green dyadic (3), in the real-valued spherical vector waves

$$\mathbf{G}(\mathbf{r}_1, \mathbf{r}_2) = -jk \sum_{\alpha} \mathbf{u}_{\alpha}^{(1)}(k\mathbf{r}_{<}) \mathbf{u}_{\alpha}^{(4)}(k\mathbf{r}_{>}) \quad (6)$$

where $\mathbf{r}_{<} = \mathbf{r}_1$ and $\mathbf{r}_{>} = \mathbf{r}_2$ if $|\mathbf{r}_1| < |\mathbf{r}_2|$, and $\mathbf{r}_{<} = \mathbf{r}_2$ and $\mathbf{r}_{>} = \mathbf{r}_1$ if $|\mathbf{r}_1| > |\mathbf{r}_2|$. The regular and outgoing spherical vector waves [12], [16]–[18] are $\mathbf{u}_{\alpha}^{(1)}(k\mathbf{r}_{<})$ and $\mathbf{u}_{\alpha}^{(4)}(k\mathbf{r}_{>})$, see Appendix B. The mode index α for real-valued spherical vector waves is [18], [19]

$$\alpha(\tau, \sigma, m, l) = 2(l^2 + l - 1 + (-1)^s m) + \tau \quad (7)$$

with $\tau \in \{1, 2\}$, $m \in \{0, \dots, l\}$, $l \in \{1, \dots, L\}$, $s = 0$ for even azimuth functions ($\sigma = e$), and $s = 1$ for odd azimuth functions ($\sigma = o$). Inserting the spherical vector waves expansion of the Green dyadic (6) into (5), the impedance matrix \mathbf{Z} becomes

$$Z_{pq} = k^2 Z_0 \sum_{\alpha} \int_{\Omega} \int_{\Omega} \psi_p(\mathbf{r}_1) \cdot \mathbf{u}_{\alpha}^{(1)}(k\mathbf{r}_{<}) \mathbf{u}_{\alpha}^{(4)}(k\mathbf{r}_{>}) \cdot \psi_q(\mathbf{r}_2) dS_1 dS_2. \quad (8)$$

For a PEC structure the resistive part of (8) can be factorized as

$$R_{pq} = k^2 Z_0 \sum_{\alpha} \int_{\Omega} \psi_p(\mathbf{r}_1) \cdot \mathbf{u}_{\alpha}^{(1)}(k\mathbf{r}_1) dS_1 \int_{\Omega} \mathbf{u}_{\alpha}^{(1)}(k\mathbf{r}_2) \cdot \psi_q(\mathbf{r}_2) dS_2 \quad (9)$$

where $\mathbf{u}_{\alpha}^{(1)}(k\mathbf{r}) = \text{Re}\{\mathbf{u}_{\alpha}^{(4)}(k\mathbf{r})\}$. Reactance matrix, \mathbf{X} , cannot be factorized in a similar way as two separate spherical waves occur.

Resistance matrix can be written in matrix form as

$$\mathbf{R} = \mathbf{S}^T \mathbf{S}, \quad (10)$$

where T is the matrix transpose. Individual elements of the matrix \mathbf{S} are

$$S_{\alpha p} = k\sqrt{Z_0} \int_{\Omega} \psi_p(\mathbf{r}) \cdot \mathbf{u}_{\alpha}^{(1)}(k\mathbf{r}) dS \quad (11)$$

and the size of the matrix \mathbf{S} is $N_{\alpha} \times N_{\psi}$, where

$$N_{\alpha} = 2L(L + 2) \quad (12)$$

is the number of spherical modes and L the highest order of spherical mode, see Appendix B. For complex-valued spherical vector waves [18] the transpose T in (10) is replaced with the hermitian transpose H . The individual integrals in (8) are in fact related to the T-matrix method [17], [20], where the incident and scattered electric fields are expanded using regular and outgoing spherical vector waves, respectively.

The radiated far-field $\mathbf{F}(\hat{\mathbf{r}})$ can conveniently be computed using spherical vector harmonics, and the matrix \mathbf{S} as

$$\mathbf{F}(\hat{\mathbf{r}}) = \frac{1}{k} \sum_{\alpha} j^{l-\tau+2} f_{\alpha} \mathbf{Y}_{\alpha}(\hat{\mathbf{r}}), \quad (13)$$

where $\mathbf{Y}_{\alpha}(\hat{\mathbf{r}})$ are the real-valued spherical vector harmonics, see Appendix B, and the expansion coefficients f_{α} are given by

$$[f_{\alpha}] = \mathbf{S} \mathbf{I}, \quad (14)$$

where the column matrix \mathbf{I} contains the current density coefficients I_p . The total time-averaged radiated power of a lossless antenna can be expressed as a sum of expansion coefficients

$$P_{\tau} \approx \frac{1}{2} \mathbf{I}^H \mathbf{R} \mathbf{I} = \frac{1}{2} |\mathbf{S} \mathbf{I}|^2 = \frac{1}{2} \sum_{\alpha} |f_{\alpha}|^2. \quad (15)$$

C. Numerical Considerations

The spectrum of the matrices \mathbf{R} and \mathbf{X} differ considerably [8], [11]. The eigenvalues of the \mathbf{R} matrix decrease exponentially and are limited by numerical noise, while this is not the case for the matrix \mathbf{X} . As a result, if the matrix \mathbf{R} is used, only a few modes can be extracted. This major limitation can be overcome with the use of the matrix \mathbf{S} in (11), whose elements vary several order of magnitude, as the result of the increased order of spherical modes with increasing row number. If the matrix \mathbf{R} is directly computed with the matrix product (10) or equivalently from matrix produced by (5) small

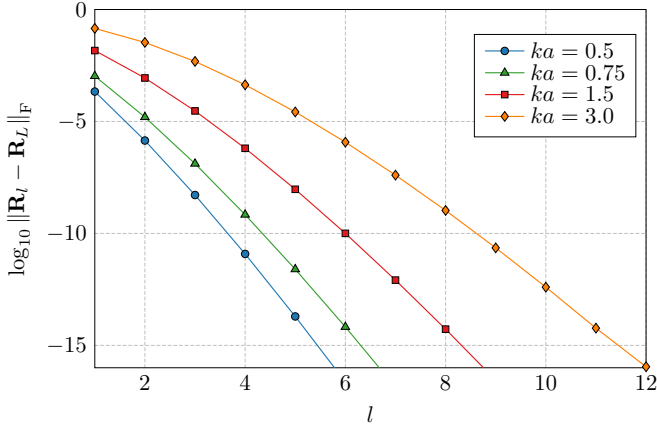


Fig. 1. Convergence of the matrix $\mathbf{R}_l = \mathbf{S}_l^T \mathbf{S}_l$ to the matrix $\mathbf{R}_L = \mathbf{S}_L^T \mathbf{S}_L$ on the rectangular plate (Example #5) for different order of spherical modes $l = \{1, \dots, L\}$ and multiple electric sizes $ka \in \{0.5, 0.75, 1.5, 3.0\}$, with the highest spherical mode order $L = 12$. The superscript F denotes the Frobenius norm. The convergence is computed with quadruple precision using the mpmath Python library [23].

values are truncated due to floating-point arithmetic¹ [21], [22]. Subsequently, the spectrum of the matrix \mathbf{R} should be found by preserving the numerical range of the matrix \mathbf{S} as presented in Section III.

The matrix \mathbf{S} also provides a low-rank matrix approximation of the matrix \mathbf{R} . This is the result of the quick convergence of regular spherical waves where usually $L_{\max} \approx ka + C$ order of modes is required, a being the radius of the sphere enclosing the scatterer and C a small number typically 10 [18]. Fig. 1 shows the convergence of the matrix \mathbf{R} for Example #5.

Substitution of the spherical vector waves, introduced in Section II-B, separates (5) into two separate surface integrals reducing computational complexity. Table I presents computation times² of different matrices³ \mathbf{Z} , \mathbf{R} , \mathbf{S} , and $\mathbf{S}^T \mathbf{S}$ for the examples given in Table II. As expected, the matrix \mathbf{Z} requires the most computational resources, as it includes both the matrix \mathbf{R} and \mathbf{X} . The computation of the matrix \mathbf{R} using MoM is faster than the matrix \mathbf{Z} since the underlying integrals are regular. The computation of the matrix \mathbf{R} using (10) is the quickest for most of the examples. The computational gain is notable for structures with more degrees-of-freedom (d-o-f), N_ψ .

III. MODAL DECOMPOSITION WITH THE MATRIX \mathbf{S}

Modal decomposition using the matrix \mathbf{S} is applied to two structures; a spherical shell of radius a (Fig. 2), and a rectangular plate of length L and width $W = L/2$ (Fig. 3), presented in Table II. Both structures are investigated for different number of d-o-f, RWG functions [25] are used as the basis functions ψ_p . The matrices used in modal decomposition have been computed using in-house solvers AToM [26]

¹As an example to the loss of significance in double precision arithmetic consider the sum $1.0 + 1 \times 10^{-30} = 1.0$.

²Computations are done on a workstation with i7-3770 CPU @ 3.4 GHz and 32 GB RAM, operating under Windows 7.

³Computation time for the \mathbf{X} matrix is omitted as it takes longer than the \mathbf{R} matrix, due to Green function singularity.

| Example (see Table II) | Time to assemble matrices in IDA (s) | | | |
|---------------------------|--------------------------------------|--------------|--------------|--|
| | \mathbf{Z} | \mathbf{R} | \mathbf{S} | $\mathbf{R} = \mathbf{S}^T \mathbf{S}$ |
| #1 | 2.62 | 0.09 | 0.036 | 0.045 |
| #3 | 14.12 | 1.77 | 0.149 | 0.315 |
| #5 | 2.34 | 0.07 | 0.019 | 0.024 |
| #6 | 11.10 | 1.11 | 0.072 | 0.136 |

TABLE I
TIME TO ASSEMBLE MATRICES IN IDA. SIMULATION SETUP FOR THE EXAMPLES ARE IN TABLE II, $N_q = 4$, MATRIX MULTIPLICATION $\mathbf{S}^T \mathbf{S}$ IS PERFORMED WITH DGEMM FROM THE INTEL MKL LIBRARY [24].

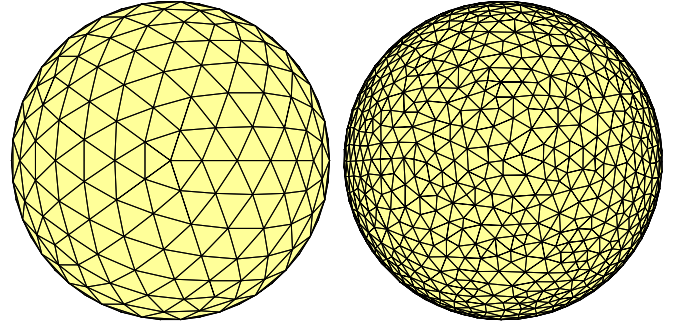


Fig. 2. Spherical shell mesh with 500 triangles (left) and 2220 triangles (right) with 750 (left) and 3330 (right) RWG basis functions, respectively. The same mesh grids are used in [11] to make the results comparable.

and IDA [27], see Appendix A for details. Results from the commercial electromagnetic solver FEKO [28] are also presented for comparison. Computations that require a higher precision than the double precision arithmetic are performed using the mpmath Python library [23], and the Advanpix Matlab toolbox [29].

A. Radiation Modes

The eigenvalues for the radiation modes [31] are easily found using the eigenvalue problem

$$\mathbf{R} \mathbf{I}_p = \xi_p \mathbf{I}_p, \quad (16)$$

where ξ_p are the eigenvalues of the matrix \mathbf{R} , and \mathbf{I}_p are the eigencurrents. The symmetry and indefiniteness of the matrix \mathbf{R} pose a problem in the eigenvalue decomposition (16) as illustrated in [8], [11]. In this paper we show that the indefiniteness caused by the numerical noise can be bypassed using the matrix \mathbf{S} . We start with the singular value decomposition (SVD) of the matrix \mathbf{S}

$$\mathbf{S} = \mathbf{U} \mathbf{\Lambda} \mathbf{V}^H, \quad (17)$$

where \mathbf{U} and \mathbf{V} are unitary matrices, and $\mathbf{\Lambda}$ is a diagonal matrix containing singular values of \mathbf{S} . Inserting (10), (17) into (16) and multiplying the left with \mathbf{V}^H yields

$$\mathbf{\Lambda}^H \mathbf{\Lambda} \tilde{\mathbf{I}}_p = \xi_p \tilde{\mathbf{I}}_p \quad (18)$$

where the eigenvectors are rewritten as $\tilde{\mathbf{I}}_p \equiv \mathbf{V}^H \mathbf{I}_p$, and the eigenvalues are $\xi_p = \Lambda_{pp}^2$.

To compare the eigenvalues ξ_p of different mesh grids, the MoM matrices have to be normalized. The normalized

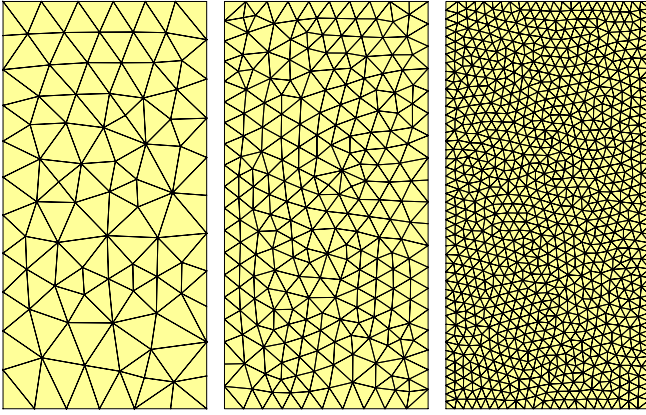


Fig. 3. Rectangular plate mesh with 144, 456, and 1818 triangles (from left to right) with 199, 655, and 2657 RWG basis functions, respectively.

| Structure | Example | ka | N_ψ | N_α |
|--|---------|------|----------|------------|
| Spherical shell (see Fig. 2) | #1 | 1/2 | 750 | 880 |
| | #2 | 3/2 | 750 | 880 |
| | #3 | 1/2 | 3330 | 880 |
| Rectangular plate (see Fig. 3) ($L/W = 2$) | #4 | 1/2 | 199 | 510 |
| | #5 | 1/2 | 655 | 510 |
| | #6 | 1/2 | 2657 | 1920 |

TABLE II

SUMMARY OF EXAMPLES USED THROUGHOUT THE PAPER, ka IS THE ELECTRICAL SIZE, N_ψ IS THE NUMBER OF BASIS FUNCTIONS (4), AND N_α IS NUMBER OF SPHERICAL MODES CALCULATED AS (12). THE ORDER OF THE SYMMETRIC QUADRATURE RULE USED TO COMPUTE THE NON-SINGULAR INTEGRALS IN (5) IS $N_q = 3$ [30].

matrices are $\hat{\mathbf{R}} = \mathbf{LRL}$, $\hat{\boldsymbol{\xi}} = \mathbf{L}\boldsymbol{\xi}\mathbf{L}$, $\hat{\mathbf{S}} = \mathbf{SL}$, $\hat{\mathbf{I}}_p = \mathbf{L}^{-1}\mathbf{I}_p$, where \mathbf{L} is the diagonal matrix of basis functions' reciprocal edge lengths, *i.e.*, $L_{pp} = 1/l_p$.

The advantage of using (18) to compute the radiation modes is illustrated in Fig. 4 for a spherical shell (Example #1). It can be seen that the number of modes computed using (18) is significantly higher compared to (16). The number of computed modes can be extended further by using quadruple precision to compute the SVD of the matrix \mathbf{S} . The results are similar for the rectangular plate (Example #5) illustrated in Fig. 5. The number of correct modes are shown in Table III for all the examples.

B. Characteristic Modes (CMs)

The generalized eigenvalue problem (GEP) with the matrix \mathbf{R} on the right hand side, *i.e.*, serving as a weighting operator [32], is much more involved as the problem cannot be completely substituted by the SVD. Yet, the SVD of the matrix \mathbf{S} in (17) plays an important role in the CM decomposition.

The CM decomposition is defined here with a GEP as

$$\mathbf{X}\mathbf{I}_p = \lambda_p \mathbf{R}\mathbf{I}_p, \quad (19)$$

which is known to suffer from limited numerical dynamics [11], therefore delivering only a limited number of modes.

| Example (see Table II) | Number of properly calculated modes | | | | |
|---------------------------|--|------|---|--|-----------------|
| | $\mathbf{R}\mathbf{I} = \boldsymbol{\xi}_p \mathbf{I}_p$ | | $\mathbf{X}\mathbf{I}_p = \lambda_p \mathbf{R}\mathbf{I}_p$ | | |
| | (16) | (18) | (19) | $\mathbf{R} = \mathbf{S}^T \mathbf{S}$ | (23) |
| #1 | 59 | 284 | 70 (5) | 96 (6) | 284 (11) |
| #2 | 96 | 364 | 105 (6) | 197 (9) | 389 (13) |
| #3 | 59 | 311 | 70 (5) | 96 (6) | 306 (11) |
| #4 | 31 | 109 | 29 | 35 | 37 |
| #5 | 29 | 117 | 26 | 33 | 98 |
| #6 | 28 | 116 | 22 | 26 | 98 |

TABLE III

COMPARISON OF THE NUMBER OF MODES CORRECTLY FOUND BY THE CLASSICAL AND THE NOVEL METHODS FOR EXAMPLES LISTED IN TABLE II. COLUMNS 2–3 SUMMARIZE THE RADIATION MODES AND COLUMNS 4–6 SUMMARIZE THE CMS. VALUES IN PARENTHESES DEPICTS THE NUMBER OF NON-DEGENERATED TM AND TE MODES FOUND ON SPHERICAL SHELL. THE MAIN OUTCOME OF THE TABLE, COMPARISON OF THE CMS IS HIGHLIGHTED BY BOLD TYPE.

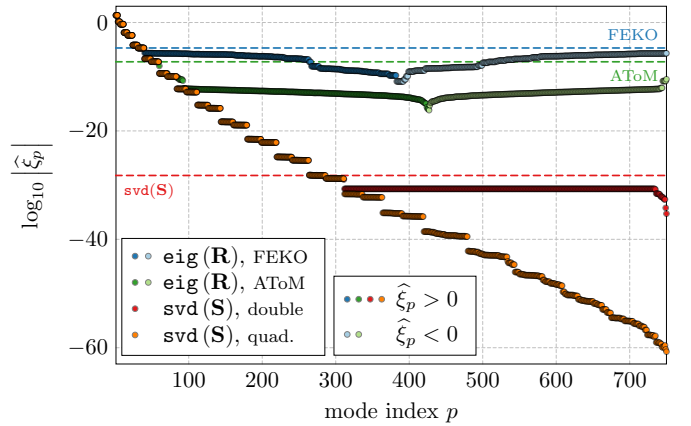


Fig. 4. Normalized eigenvalues of the matrix \mathbf{R} of a spherical shell with electrical size $ka = 0.5$ discretized into 500 triangles (Example #1). Multiprecision package Advanpix [29] has been used for evaluation in quadruple precision. The number of well-determined modes is delimited by horizontal dashed lines.

The first step is to represent the solution in a basis of singular vectors \mathbf{V} by substituting the matrix \mathbf{R} in (19) as (10), with (17) and multiplying (19) from the left by the matrix \mathbf{V}^H

$$\mathbf{V}^H \mathbf{X} \mathbf{V} \mathbf{V}^H \mathbf{I}_p = \lambda_p \boldsymbol{\Lambda}^H \boldsymbol{\Lambda} \mathbf{V}^H \mathbf{I}_p. \quad (20)$$

Formulation (20) can formally be expressed as a GEP with an already diagonalized right hand side [33]

$$\tilde{\mathbf{X}}\tilde{\mathbf{I}}_p = \lambda_p \tilde{\mathbf{R}}\tilde{\mathbf{I}}_p, \quad (21)$$

i.e., $\tilde{\mathbf{X}} \equiv \mathbf{V}^H \mathbf{X} \mathbf{V}$, $\tilde{\mathbf{R}} \equiv \boldsymbol{\Lambda}^H \boldsymbol{\Lambda}$, and $\tilde{\mathbf{I}}_p \equiv \mathbf{V}^H \mathbf{I}_p$.

Since the matrix \mathbf{S} is in general rectangular, it is crucial to take into account cases where $N_\alpha < N_\psi$. This is equivalent to a situation in which there are limited number of spherical projections to recover the CMs. Consequently, only limited number of singular values Λ_{pp} exist. In such a case, the procedure similar to the one used in [34] should be undertaken by partitioning (21) into two linear systems

$$\tilde{\mathbf{X}}\tilde{\mathbf{I}} = \begin{pmatrix} \tilde{\mathbf{X}}_{11} & \tilde{\mathbf{X}}_{12} \\ \tilde{\mathbf{X}}_{21} & \tilde{\mathbf{X}}_{22} \end{pmatrix} \begin{pmatrix} \tilde{\mathbf{I}}_{1p} \\ \tilde{\mathbf{I}}_{2p} \end{pmatrix} = \begin{pmatrix} \lambda_{1p} \tilde{\mathbf{R}}_{11} \tilde{\mathbf{I}}_{1p} \\ \mathbf{0} \end{pmatrix} \quad (22)$$

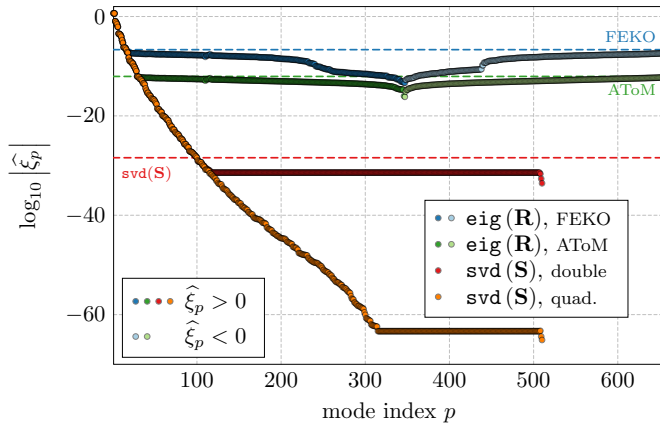


Fig. 5. Normalized eigenvalues of the matrix \mathbf{R} of rectangular plate (Example #5). Since the matrix \mathbf{S} has only 510 rows, the number of modes is limited. The number of well-determined modes is delimited by horizontal dashed lines.

where $\tilde{\mathbf{I}}_{1p} \in \mathbb{C}^{N_\alpha}$, $\tilde{\mathbf{I}}_{2p} \in \mathbb{C}^{N_\psi - N_\alpha}$, and $N_\alpha < N_\psi$. The Schur complement is obtained by substituting the second row of (22) into the first row

$$\left(\tilde{\mathbf{X}}_{11} - \tilde{\mathbf{X}}_{12} \tilde{\mathbf{X}}_{22}^{-1} \tilde{\mathbf{X}}_{21} \right) \tilde{\mathbf{I}}_{1p} = \lambda_{1n} \tilde{\mathbf{R}}_{11} \tilde{\mathbf{I}}_{1p} \quad (23)$$

with expansion coefficients of CMs defined as

$$\tilde{\mathbf{I}}_p = \begin{pmatrix} \tilde{\mathbf{I}}_{1p} \\ -\tilde{\mathbf{X}}_{22}^{-1} \tilde{\mathbf{X}}_{21} \tilde{\mathbf{I}}_{1p} \end{pmatrix}. \quad (24)$$

As far as the matrices \mathbf{U} and \mathbf{V} in (17) are unitary, the decomposition (21) yields CMs implicitly normalized to

$$\tilde{\mathbf{I}}_p^H \tilde{\mathbf{R}} \tilde{\mathbf{I}}_q = \delta_{pq}, \quad (25)$$

which is crucial since the standard normalization cannot be used without decreasing the numerical dynamics. In order to demonstrate the use of (23), various examples from Table II are calculated and compared with the conventional approach (19).

The CMs of the spherical shell from Example #1 are calculated and shown as absolute values in logarithmic scale in Fig. 6. It is shown that the number of the CMs calculated by classical procedure (FEKO, AToM) is limited to the lower modes, especially considering the degeneracy $2l + 1$ of the CMs on the spherical shell [11]. The number of properly found CMs is significantly higher when using (23) than the conventional approach (19) and numerical dynamics are doubled. Notice that, even (19) where the matrix \mathbf{R} calculated from (10) yields slightly better results than the conventional procedure. This fact is confirmed in Fig. 7 dealing with Example #5, where the multiprecision package Advanpix is used as a reference. The same calculation proves that the matrix \mathbf{R} contains all information to recover the same number of modes as (23), but this can be done only at the expense of higher computational time, see Table IV. Two tests proposed in [11] are performed to validate the conformity of characteristic current densities and the characteristic far fields with the analytically known values. The results of the former test are depicted in Fig. 8 for Example #1 and #3 that are spherical

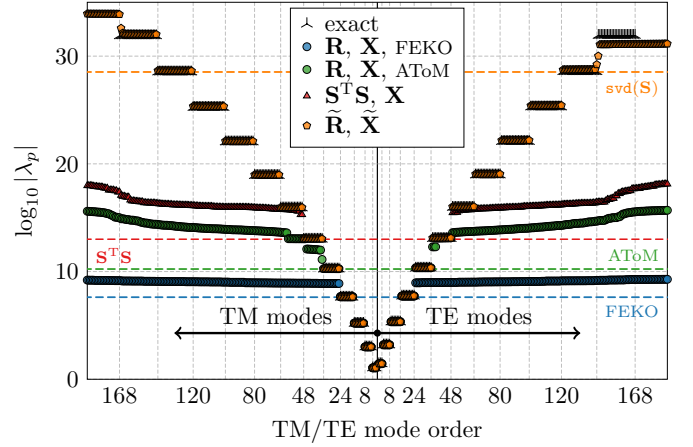


Fig. 6. The absolute values of the CMs of spherical shell with electrical size $ka = 0.5$ (Example #1). Data calculated with classical procedure (19) are compared with techniques from this paper, (20), (23), and with the analytical results valid for the spherical shell [11].

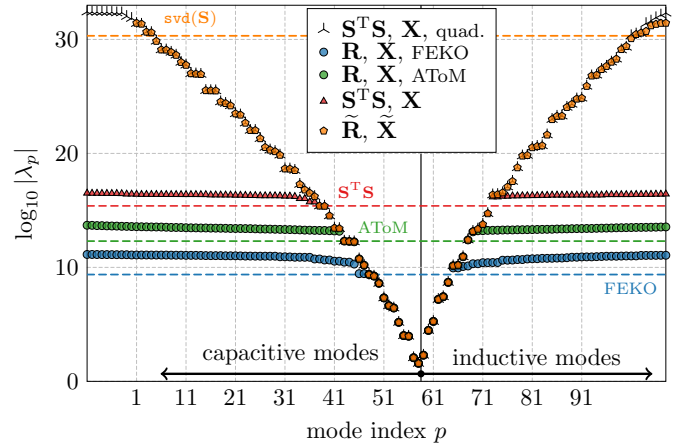


Fig. 7. The absolute values of the CMs of rectangular plate (Example #5). Since unknown analytical results, the multiprecision package Advanpix has been used instead to calculate the first 150 modes from impedance matrix in quadruple precision.

shells with two different d-o-f. Similarity coefficients $\chi_{\tau n}$ are depicted both for the CMs using the matrix \mathbf{R} (19) and for the CMs calculated by (23). The number of valid modes correlates well with Table III and the same dependence on the quality and size of the mesh grid as in [11] is observed.

Qualitatively the same behavior is also observed in the latter test, depicted in Fig. 9. The similarity of the characteristic far fields, expressed by coefficient $\zeta_{\tau n}$ [11], were slightly modified here to preserve the numerical dynamics of the calculated characteristic far fields. The coefficients read

$$\zeta_{\tau n} = \frac{\max_l \sum_{\sigma m} |P_{\sigma n}|^2}{\sum_{\alpha} |P_{\alpha n}|^2}, \quad (26)$$

| Example (see Table II) | N_λ | Time to calculate N_λ CMs (s) | | | |
|---------------------------|-------------|---------------------------------------|--|------------|-----------------|
| | | (19) | $\mathbf{R} = \mathbf{S}^T \mathbf{S}$ | (23) | (19) & Advanpix |
| #1 | 300 | 5.5 | 2.9 | 2.5 | 53334.4 |
| #4 | 100 | 0.7 | 0.7 | 0.5 | 1324.8 |

TABLE IV

COMPARISON OF COMPUTATIONAL TIME REQUIRED BY VARIOUS METHODS CAPABLE TO CALCULATE FIRST N_λ CMs. ONLY THE METHODS IN THE LAST TWO COLUMNS (HIGHLIGHTED BY BOLD TYPE) ARE ABLE TO CALCULATE REQUIRED MODES PROPERLY. THE MULTIPRECISION PACKAGE ADVANPIX WAS USED TO CALCULATE DECOMPOSITION (19) USING QUADRUPLE PRECISION. THE CALCULATIONS WERE DONE ON WINDOWS SERVER 2012 WITH 2×XEON E5-2665 CPU @ 2.4 GHz AND 72 GB RAM.

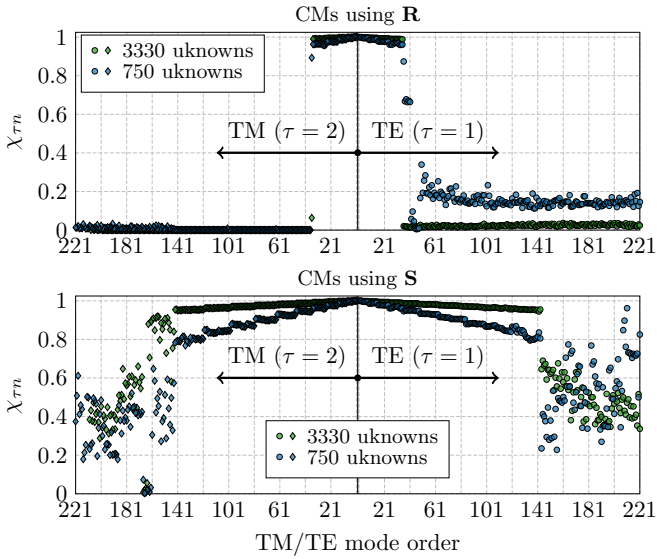


Fig. 8. Similarity of numerically evaluated characteristic currents for a spherical shell of two different discretizations (Example #1 and #3) and the analytically known currents [11]. The coefficients $\chi_{\tau n}$ were calculated according to [11], top panel depicts results for the conventional procedure (19), bottom panel for the procedure from this paper (23).

where

$$P_{\alpha n} = \frac{1}{2Z_0} \int_0^{2\pi} \int_0^\pi \mathbf{Y}_\alpha(\hat{\mathbf{r}}) \cdot \mathbf{F}_p(\hat{\mathbf{r}}) \sin \vartheta \, d\vartheta \, d\varphi \quad (27)$$

with \mathbf{F}_p being the characteristic far fields evaluated for a spherical shell using (13) with $[\tilde{\mathbf{f}}_\alpha] = \mathbf{S}\mathbf{I}_p$. The characteristic far fields computed from the conventional procedure (19) and the procedure presented in this paper (23) are illustrated in Fig. 9.

Lastly, practical advantages of using (23) over (19), are demonstrated in the Fig. 10, comparing the 41st CM of the rectangular plate (Example #5). The surface current density in the left panel, calculated using \mathbf{I}_{41} in (19) is, in fact, only the numerical noise. However, in the right panel, the current density calculated by (23) corresponds to some of the higher-order modes. Refining the mesh grid, even higher modes can be calculated with (23), see Fig. 11. These higher-order modes can be utilized for specialized applications covering antenna

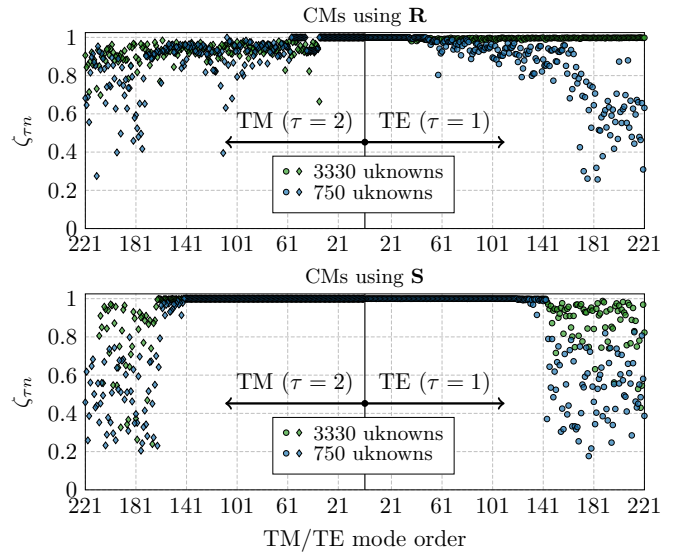


Fig. 9. Similarity of numerically and analytically evaluated characteristic far fields for a spherical shell of two different discretizations (Example #1 and #3) and analytically known far fields [11]. The coefficients $\zeta_{\tau n}$ were calculated according to [11], top panel depicts results for the conventional procedure (19), bottom panel for the procedure from this paper (23).

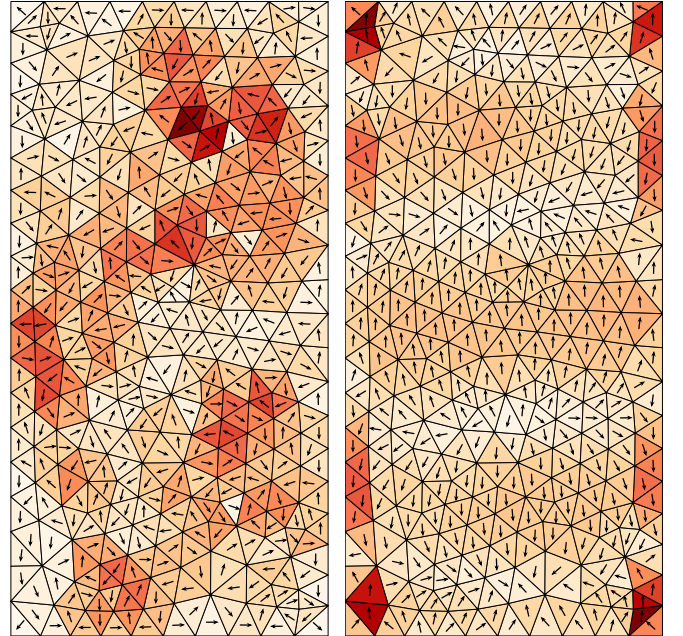


Fig. 10. Comparison of the 41st CM of the rectangular plate (Example #5), left panel: conventional procedure (19), right panel: procedure from this paper (23).

arrays, electrically large structures, numerical benchmarks, or precise tracking algorithms.

IV. DISCUSSION

Important aspects of the utilization of the matrix \mathbf{S} are discussed under independent headings, covering the theory, numerical treatments, and potential improvements to be considered for the future.

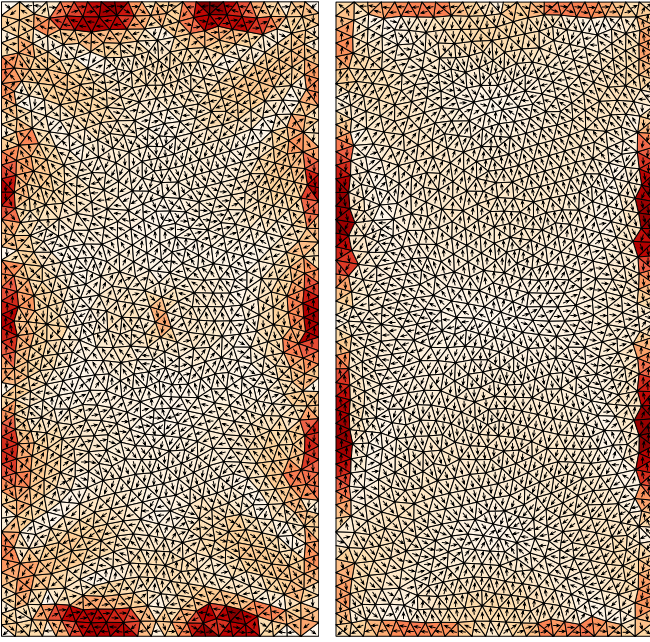


Fig. 11. Two high-order modes of rectangular plate (Example #6), found by procedure from this paper. Mode in the left panel is capacitive with $\lambda_{77} = -1.947 \cdot 10^{24}$, mode in the right panel is inductive with $\lambda_{17} = 2.461 \cdot 10^{17}$.

A. Physical Meaning and Usefulness

Unlike the reactance matrix \mathbf{X} , the resistance matrix \mathbf{R} suffers from high condition number. This fact is a direct consequence of only a small number of well-radiating (spherical) modes, especially notable in the electrically small regime. Therefore, the combined approach to evaluate the impedance matrix (matrix \mathbf{R} using matrix \mathbf{S} , matrix \mathbf{X} using conventional Green function technique with double integration) takes advantages of both methods and seems to be optimal for, *e.g.*, modal decomposition techniques dealing with the matrix \mathbf{R} (radiation modes [31], CMs, energy modes [31], [35], and solution of optimization problems [36]). Evaluation and the SVD of the matrix \mathbf{S} are also used to estimate number of modes, *cf.* number of modes of the matrix \mathbf{S} found by (17) and number of CMs found by (23) in Table III.

Evaluation of the matrix \mathbf{S} is done only for source current in free-space. This requirement is, however, quite common in the context of the modal methods: the CMs are originally defined exclusively in free-space as the far fields have to be orthogonal [37].

The fact that all modes cannot be recovered even with specialized techniques poses a question about completeness of the modal bases. This theoretical problem is left aside in this paper as it has been observed that the number of properly found modes is strictly limited by the number of projections N_α , the number of basis functions N_ψ , the electrical size ka , and, for particular numerical procedure, by limited numerical dynamics. Therefore, the completeness of the modes is far from being granted, which introduces serious problems for applications that require a complete basis, *e.g.* in selective excitation of modes.

B. Computational Aspects

Computational gains of the proposed method presented in Table I can be interpreted in two ways: either the same amount of modes can be calculated faster than the conventional approach, or a (significantly) higher number of modes can be calculated investing the same amount of computational time as the conventional method.

Importantly, convergence requirements summarized in Fig. 1 can be met easily. Subsequently, only spherical Bessel functions up to the order $L = 12$ are needed to get double precision matching between matrices \mathbf{R} and $\mathbf{S}^T \mathbf{S}$ even for relatively high frequencies ($ka = 3$).

An advantage of the proposed method is that the matrix \mathbf{S} is rectangular for $N_\alpha < N_\psi$, allowing independent selection of the parameters N_ψ and N_α . While the parameter N_ψ controls the details in the model, the parameter N_α (or alternatively L) controls the convergence of the matrix \mathbf{S} and the number of modes to be found. Notice that the parameter N_α is limited from below by the convergence and the number of desired modes, but also from above since spherical Bessel function in $\mathbf{u}_\alpha^{(1)}(kr)$ decays rapidly with l as

$$j_l(ka) \approx \frac{2^l l!}{(2l+1)!} (ka)^l, \quad ka \rightarrow 0. \quad (28)$$

C. Potential Improvements

Even though the numerical dynamics are remarkably improved, they are strictly limited and present an inevitable, thus fundamental, bottleneck of all modal methods involving radiation properties. The true technical limitation is the SVD of the matrix \mathbf{S} . A possible remedy is the use of high-precision packages that come at an expense of markedly longer computation times and the necessity of performing all subsequent operations in the same package to preserve high numerical precision.

The second potential improvement relies on higher-order basis functions, which can compensate poor-meshing scheme (which is sometimes unavoidable for complex or electrically large models). It can also reduce the number of basis function N_ψ so that the evaluation of (11), (10), and (17) are further accelerated.

V. CONCLUSION

Evaluation of the discretized form of the EFIE impedance operator, the impedance matrix, has been reformulated using projection of spherical harmonics onto a set of basis functions representing the radiator. The key feature of the proposed method is the fact that the real part of the impedance matrix can be written as a multiplication of the spherical modes projection matrix with itself. This feature opens new possibilities in a wide area of modal decomposition techniques given that the achievable numerical dynamics are doubled. Consequently, the proposed method resolves a class of fundamental problems of CM decomposition.

The approach presented here opens new ways to deal with complicated examples, *i.e.*, geometrically complex shapes, electrically large structures, or symmetrical bodies. Moreover,

the approach may also improve performance of tracking algorithms and feeding synthesis, essential tools for modal decomposition techniques.

For radiators located in free-space, the proposed method leads to faster evaluation and higher number of modes properly found as compared with the conventional procedure. The method is of particular interest for all cases in which the number of desired modes is high including small antenna analysis, design of antenna arrays, and antenna synthesis in general. The results obtained by the method can also be used as reference for validation and benchmarking. These facts have been confirmed via comparison with analytically known results. Additionally, the doubled numerical dynamics lead to roughly four times more modes.

It has been shown that the method has notable advantages, namely the number of available modes can be estimated prior to the decomposition and the convergence can be controlled via the number of basis functions and the number of projections. The normalization of generalized eigenvalue problems with respect to the product of the spherical modes projection matrix on the right hand side are implicitly done. The presented procedure finds its use in various optimization techniques as well. It allows for example to prescribe the radiation pattern of optimized current by restricting the set of the spherical harmonics used for construction of the matrix.

The method can be straightforwardly implemented into both in-house and commercial solvers, improving thus their performance and providing antenna designers with more accurate and larger sets of modes.

APPENDIX A

USED COMPUTATIONAL ELECTROMAGNETICS PACKAGES

A. FEKO

FEKO (ver. 14.0-273612, [28]) has been used with a mesh structure that was imported in NASTRAN file format [38]; CMs and far fields were chosen from the model tree under *requests* for the FEKO solver. Data from FEKO were acquired using *.out, *.os, *.mat and *.ffe files. The impedance matrices were imported using an in-house wrapper [27]. Double precision was enabled for data storage in solver settings.

B. AToM

AToM (pre-product ver., CTU in Prague, [26]) has been used with a mesh grid that was imported in NASTRAN file format [38], and simulation parameters were set to comply with the data in Table II. AToM uses RWG basis functions with the Galerkin procedure [25]. The Gaussian quadrature is implemented according to [30] and singularity treatment is implemented from [39]. Built-in Matlab functions are utilized for matrix inversion and decomposition. Multiprecision package Advanpix [29] is used for comparison purposes.

C. IDA

IDA (in-house, Lund University, [27]) has been used with the NASTRAN mesh and processed with the IDA geometry interpreter. IDA solver is a Galerkin type MoM implementation.

RWG basis functions are used for the current densities. Numerical integrals are performed using Gaussian quadrature [30] for non-singular terms and the DEMCEM library [40] for singular terms. Intel MKL library [24] is used for linear algebra routines. The matrix computation routines are parallelized using OpenMP 2.0 [41]. Multiprecision computations were done with the mpmath Python library [23].

APPENDIX B SPHERICAL VECTOR WAVES

General expression of the (scalar) spherical modes is [12]

$$\mathbf{u}_{\sigma ml}^{(p)}(k\mathbf{r}) = z_l^{(p)}(kr) \mathbf{Y}_{\sigma ml}(\hat{\mathbf{r}}), \quad (29)$$

with $\hat{\mathbf{r}} = \mathbf{r}/|\mathbf{r}|$ and k being the wavenumber. The indices are $m \in \{0, \dots, l\}$, $\sigma \in \{e, o\}$ and $l \in \{1, \dots, L\}$ [18], [19]. For regular waves $z_l^{(1)} = j_l$ is a spherical Bessel function of order l , irregular waves $z_l^{(2)} = n_l$ is a spherical Neumann function, and $z_l^{(3,4)} = h_l^{(1,2)}$ are spherical Hankel functions for the ingoing and outgoing waves, respectively. Spherical harmonics are defined as [12]

$$\mathbf{Y}_{\sigma ml}(\hat{\mathbf{r}}) = \sqrt{\frac{\varepsilon_m}{2\pi}} \tilde{P}_l^m(\cos \vartheta) \begin{Bmatrix} \cos m\varphi \\ \sin m\varphi \end{Bmatrix}, \quad \sigma = \begin{Bmatrix} e \\ o \end{Bmatrix} \quad (30)$$

with $\varepsilon_m = 2 - \delta_{m0}$ the Neumann factor, δ_{ij} the Kronecker delta function and $\tilde{P}_l^m(\cos \vartheta)$ the normalized associated Legendre functions [42].

The real-valued spherical vector waves are [12], [18]

$$\mathbf{u}_{1\sigma ml}^{(p)}(k\mathbf{r}) = R_{1l}^{(p)}(kr) \mathbf{Y}_{1\sigma ml}(\hat{\mathbf{r}}), \quad (31a)$$

$$\mathbf{u}_{2\sigma ml}^{(p)}(k\mathbf{r}) = R_{2l}^{(p)}(kr) \mathbf{Y}_{2\sigma ml}(\hat{\mathbf{r}}) + R_{3l}^{(p)}(kr) \mathbf{Y}_{\sigma ml}(\hat{\mathbf{r}}) \hat{\mathbf{r}}, \quad (31b)$$

where $R_{\tau l}^{(p)}(kr)$ are the radial function of order l defined as

$$R_{\tau l}^{(p)}(\kappa) = \begin{cases} z_l^{(p)}(\kappa), & \tau = 1, \\ \frac{1}{\kappa} \frac{\partial}{\partial \kappa} (\kappa z_l^{(p)}(\kappa)), & \tau = 2, \\ \frac{b_l}{\kappa} z_l^{(p)}(\kappa), & \tau = 3, \end{cases} \quad (32a)$$

$$\tau = 2, \quad (32b)$$

$$\tau = 3, \quad (32c)$$

with

$$b_l = \sqrt{l(l+1)} \quad (33)$$

and $\mathbf{Y}_{\tau\sigma ml}(\hat{\mathbf{r}})$ denotes the real-valued vector spherical harmonics defined as

$$\mathbf{Y}_{1\sigma ml}(\hat{\mathbf{r}}) = \frac{1}{b_l} \nabla \times (\mathbf{r} Y_{\sigma ml}(\hat{\mathbf{r}})), \quad (34a)$$

$$\mathbf{Y}_{2\sigma ml}(\hat{\mathbf{r}}) = \hat{\mathbf{r}} \times \mathbf{Y}_{1\sigma ml}(\hat{\mathbf{r}}), \quad (34b)$$

where $Y_{\sigma ml}$ denotes the ordinary spherical harmonics [12].

APPENDIX C ASSOCIATED LEGENDRE POLYNOMIALS

The associated Legendre functions are defined [43] as

$$P_l^m(x) = (1-x^2)^{m/2} \frac{d^m}{dx^m} P_l(x), \quad l \geq m \geq 0, \quad (35)$$

with

$$P_l(x) = \frac{1}{2^l l!} \frac{d^l}{dx^l} (x^2 - 1)^l \quad (36)$$

being the associated Legendre polynomials of degree l and $x \in [-1, 1]$. One useful limit when computing the vector spherical harmonics is [12]

$$\lim_{x \rightarrow 1} \frac{P_l^m(x)}{\sqrt{1-x^2}} = \delta_{m1} \frac{l(l+1)}{2}. \quad (37)$$

The normalized associated Legendre function \tilde{P}_l^m , is defined as follows

$$\tilde{P}_l^m(x) = \sqrt{\frac{2l+1}{2} \frac{(l-m)!}{(l+m)!}} P_l^m(x). \quad (38)$$

The derivative of the normalized associated Legendre function is required when computing the spherical harmonics, and is given by the following recursion relation

$$\begin{aligned} \frac{\partial}{\partial \vartheta} \tilde{P}_l^m(\cos \vartheta) &= \frac{1}{2} \sqrt{(l+m)(l-m+1)} \tilde{P}_l^{m-1}(\cos \vartheta) \\ &- \frac{1}{2} \sqrt{(l-m)(l+m+1)} \tilde{P}_l^{m+1}(\cos \vartheta) \end{aligned} \quad (39)$$

where $x \equiv \cos \vartheta$, $\vartheta \in [0, \pi]$.

REFERENCES

- [1] R. F. Harrington, *Field Computation by Moment Methods*. Wiley – IEEE Press, 1993.
- [2] M. N. O. Sadiku, *Numerical Techniques in Electromagnetics with Matlab*, 3rd ed. CRC Press, 2009.
- [3] G. H. Golub and C. F. Van Loan, *Matrix Computations*. Johns Hopkins University Press, 2012.
- [4] R. F. Harrington and J. R. Mautz, “Theory of characteristic modes for conducting bodies,” *IEEE Trans. Antennas Propag.*, vol. 19, no. 5, pp. 622–628, 1971.
- [5] B. Yang and J. J. Adams, “Systematic shape optimization of symmetric MIMO antennas using characteristic modes,” *IEEE Trans. Antennas Propag.*, vol. 64, no. 7, pp. 2668–2678, July 2016.
- [6] M. Capek, P. Hazdra, and J. Eichler, “A method for the evaluation of radiation Q based on modal approach,” *IEEE Trans. Antennas Propag.*, vol. 60, no. 10, pp. 4556–4567, Oct. 2012.
- [7] M. Capek and L. Jelinek, “Optimal composition of modal currents for minimal quality factor Q,” *IEEE Trans. Antennas Propag.*, vol. 64, no. 12, pp. 5230–5242, 2016.
- [8] M. Gustafsson, D. Tayli, C. Ehrenborg, M. Cismasu, and S. Norbedo, “Antenna current optimization using MATLAB and CVX,” *FERMAT*, vol. 15, no. 5, pp. 1–29, May–June 2016. [Online]. Available: <http://www.e-fermat.org/articles/gustafsson-art-2016-vol15-may-jun-005/>
- [9] M. Vogel, G. Gampala, D. Ludick, U. Jakobus, and C. Reddy, “Characteristic mode analysis: Putting physics back into simulation,” *IEEE Antennas Propag. Mag.*, vol. 57, no. 2, pp. 307–317, April 2015.
- [10] Y. Chen and C.-F. Wang, “Electrically small UAV antenna design using characteristic modes,” *IEEE Trans. Antennas Propag.*, vol. 62, no. 2, pp. 535–545, Feb. 2014.
- [11] M. Capek, V. Losenicky, L. Jelinek, and M. Gustafsson, “Validating the characteristic modes solvers,” *IEEE Trans. Antennas Propag.*, vol. 65, no. 8, pp. 4134–4145, Aug. 2017.
- [12] G. Kristensson, *Scattering of Electromagnetic Waves by Obstacles*. Edison, NJ: SciTech Publishing, an imprint of the IET, 2016.
- [13] R. F. Harrington, *Time-Harmonic Electromagnetic Fields*, 2nd ed. Wiley – IEEE Press, 2001.
- [14] W. C. Chew, M. S. Tong, and B. Hu, *Integral Equation Methods for Electromagnetic and Elastic Waves*. Morgan & Claypool, 2009.
- [15] W. C. Gibson, *The Method of Moments in Electromagnetics*. CRC press, 2014.
- [16] P. M. Morse and H. Feshbach, *Methods of Theoretical Physics*. New York, NY: McGraw-Hill, 1953, vol. 2.
- [17] P. C. Waterman, “Symmetry, unitarity, and geometry in electromagnetic scattering,” *Phys. Rev. D*, vol. 3, no. 4, pp. 825–839, 1971.
- [18] J. E. Hansen, Ed., *Spherical Near-Field Antenna Measurements*, ser. IEE electromagnetic waves series. Stevenage, UK: Peter Peregrinus Ltd., 1988, no. 26.
- [19] M. Gustafsson and S. Norbedo, “Characterization of MIMO antennas using spherical vector waves,” *IEEE Trans. Antennas Propag.*, vol. 54, no. 9, pp. 2679–2682, 2006.
- [20] P. Waterman, “Matrix formulation of electromagnetic scattering,” *Proc. IEEE*, vol. 53, no. 8, pp. 805–812, Aug. 1965.
- [21] D. Zuras, M. Cowlshaw, A. Aiken, M. Applegate, D. Bailey, S. Bass, D. Bhandarkar, M. Bhat, D. Bindel, S. Boldo *et al.*, “IEEE standard for floating-point arithmetic,” *IEEE Std 754-2008*, pp. 1–70, 2008.
- [22] R. Burden, J. Faires, and A. Burden, *Numerical Analysis*. Cengage Learning, 2015.
- [23] F. Johansson *et al.* (2013, December) mpmath: a Python library for arbitrary-precision floating-point arithmetic (version 0.18). [Online]. Available: <http://mpmath.org/>
- [24] Intel. (2017) Intel Math Kernel Library 2017 update 3. [Online]. Available: <https://software.intel.com/en-us/mkl>
- [25] S. M. Rao, D. R. Wilton, and A. W. Glisson, “Electromagnetic scattering by surfaces of arbitrary shape,” *IEEE Trans. Antennas Propag.*, vol. 30, no. 3, pp. 409–418, May 1982.
- [26] (2017) Antenna Toolbox for MATLAB (AToM). Czech Technical University in Prague. [Online]. Available: www.antennatoolbox.com
- [27] D. Tayli. (2017) IDA (Integrated Development toolset for Antennas). Lund University.
- [28] Altair. (2016) FEKO. Altair. [Online]. Available: www.feko.info
- [29] Advanpix. (2016) Multiprecision Computing Toolbox for MATLAB. [Online]. Available: <http://www.advanpix.com/>
- [30] D. A. Dunavant, “High degree efficient symmetrical gaussian quadrature rules for the triangle,” *International Journal for Numerical Methods in Engineering*, vol. 21, pp. 1129–1148, 1985.
- [31] K. R. Schab and J. T. Bernhard, “Radiation and energy storage current modes on conducting structures,” *IEEE Trans. Antennas Propag.*, vol. 63, no. 12, pp. 5601–5611, Dec. 2015.
- [32] J. H. Wilkinson, *The Algebraic Eigenvalue Problem*. Oxford University Press, 1988.
- [33] G. Angiulli and F. Venneri, “Use of the simultaneous diagonalization technique in the $Ax = \lambda Bx$ eigenproblem applied to the computation of the characteristic modes,” *ACES Journal*, vol. 17, no. 3, pp. 232–238, Nov. 2002.
- [34] R. F. Harrington and J. R. Mautz, “Computation of characteristic modes for conducting bodies,” *IEEE Trans. Antennas Propag.*, vol. 19, no. 5, pp. 629–639, Sept. 1971.
- [35] L. Jelinek and M. Capek, “Optimal currents on arbitrarily shaped surfaces,” *IEEE Trans. Antennas Propag.*, vol. 65, no. 1, pp. 329–341, Jan. 2017.
- [36] M. Capek, M. Gustafsson, and K. Schab, “Minimization of antenna quality factor,” *IEEE Trans. Antennas Propag.*, vol. 65, no. 8, pp. 4115–4123, 2017.
- [37] R. J. Garbacz and R. H. Turpin, “A generalized expansion for radiated and scattered fields,” *IEEE Trans. Antennas Propag.*, vol. 19, no. 3, pp. 348–358, May 1971.
- [38] (2017) MSC NASTRAN. [Online]. Available: <http://www.mssoftware.com/support/>
- [39] T. F. Eibert and V. Hansen, “On the calculation of potential integrals for linear source distributions on triangular domains,” *IEEE Trans. Antennas Propag.*, vol. 43, no. 12, pp. 1499–1502, Dec. 1995.
- [40] A. G. Polimeridis. (2011) Direct evaluation method in computational electromagnetics (DEMCEM) package. <http://web.mit.edu/thanos/www/Software.html>.
- [41] L. Dagum and R. Menon, “OpenMP: an industry standard api for shared-memory programming,” *Computational Science & Engineering, IEEE*, vol. 5, no. 1, pp. 46–55, 1998.
- [42] F. W. J. Olver, D. W. Lozier, R. F. Boisvert, and C. W. Clark, *NIST Handbook of mathematical functions*. New York: Cambridge University Press, 2010.
- [43] A. Jeffrey and H.-H. Dai, *Handbook of Mathematical Formulas and Integrals*, 4th ed. Academic Press, 2008.



Doruk Tayli (S'13) received his B.Sc. degree in Electronics Engineering from Istanbul Technical University and his M.Sc. in degree in Communications Systems from Lund University, in 2010 and 2013, respectively. He is currently a Ph.D. student at Electromagnetic Theory Group, Department of Electrical and Information Technology at Lund University.

His research interests are Physical Bounds, Small Antennas and Computational Electromagnetics.



Mats Gustafsson (SM'17) received the M.Sc. degree in Engineering Physics 1994, the Ph.D. degree in Electromagnetic Theory 2000, was appointed Docent 2005, and Professor of Electromagnetic Theory 2011, all from Lund University, Sweden.

He co-founded the company Phase holographic imaging AB in 2004. His research interests are in scattering and antenna theory and inverse scattering and imaging. He has written over 90 peer reviewed journal papers and over 100 conference papers. Prof. Gustafsson received the IEEE Schelkunoff Transactions Prize Paper Award 2010 and Best Paper Awards at EuCAP 2007 and 2013. He served as an IEEE AP-S Distinguished Lecturer for 2013-15.

He served as an IEEE AP-S Distinguished Lecturer for 2013-15.



Miloslav Capek (S'09, M'14) received his Ph.D. degree from the Czech Technical University in Prague, Czech Republic, in 2014. In 2017 he was appointed Associate Professor at the Department of Electromagnetic Field at the same university.

He leads the development of the AToM (Antenna Toolbox for Matlab) package. His research interests are in the area of electromagnetic theory, electrically small antennas, numerical techniques, fractal geometry and optimization. He authored or co-authored over 65 journal and conference papers.

Dr. Capek is member of Radioengineering Society, regional delegate of EurAAP, and Associate Editor of Radioengineering.



Vit Losenicky received the M.Sc. degree in electrical engineering from the Czech Technical University in Prague, Czech Republic, in 2016. He is now working towards his Ph.D. degree in the area of electrically small antennas.



Akrou Lamyae received the Dipl.-Ing. degree in networks and telecommunications from National School of Applied Sciences of Tetouan in 2012. Since 2014 she is working towards her Ph.D. degree in Electrical and Computer Engineering at the University of Coimbra.



Lukas Jelinek received his Ph.D. degree from the Czech Technical University in Prague, Czech Republic, in 2006. In 2015 he was appointed Associate Professor at the Department of Electromagnetic Field at the same university.

His research interests include wave propagation in complex media, general field theory, numerical techniques and optimization.